Lipid-Functionalized Graphene Loaded with hMnSOD for Selective Inhibition of Cancer Cells

Megan Farell^a, Ava Self^a, Christine Guza^a, Hyewon Song^a, Luigi Apollon^b, Esther W. Gomez^{a,c*}, and Manish Kumar^{a,c,d*}

^aDepartment of Chemical Engineering, The Pennsylvania State University, University Park, PA 16802, USA

^bDepartment of Chemistry and Biochemistry, Worcester Polytechnic Institute, Worcester, MA 01609, USA

^cDepartment of Biomedical Engineering, The Pennsylvania State University, University Park, PA 16802, USA

^dDepartment of Civil, Architectural, and Environmental Engineering, The University of Texas at Austin, Austin, TX, 78712, USA

*corresponding authors

ewg10@psu.edu, manish.kumar@utexas.edu

Abstract

Combination therapies utilize multiple mechanisms to target cancer cells in order to minimize cancer cell survival. Graphene provides an ideal platform for combination therapy due to its photothermal properties and high loading capacity for cancer-fighting molecules. Lipid-functionalization of graphene extends its potential as a therapeutic platform by improving its biocompatibility and functionality. Previous studies involving graphene demonstrated its usage as a therapeutic vehicle; however, the effect of bare and engineered graphene structures on oxidative stress has not been comprehensively investigated. Because oxidative stress has been linked to cancer progression, it is vital to examine generation of reactive oxygen species (ROS) in response to therapeutic platforms. This study functionalizes reduced graphene oxide (rGO) with lipids and the antioxidant enzyme human manganese superoxide dismutase (hMnSOD) and presents a detailed characterization of cellular responses to bare and functionalized rGO nanostructures in tumorigenic and non-tumorigenic breast cell lines. Each cell type displayed distinct responses depending on whether they were normal, non-metastatic, or metastatic cells. Bare rGO

significantly reduced cell growth and substantially increased ROS production in all cell lines and instigated necrosis in metastatic breast cancer cells. Cell proliferation decreased in cancerous breast cells upon introduction of lipid-rGO, which correlated with peroxidation of lipids coating the rGO. In contrast, lipid-rGO nanostructures had minimal impact on proliferation and lipid peroxidation for normal breast cells. Lipid-rGO nanostructures with bound hMnSOD inhibited proliferation of metastatic cancer cells while preventing necrosis and avoiding the negative side effects on normal cells associated with chemotherapeutic agents. Together, the results confirm the importance of functionalizing rGO for therapeutic applications and present an additional modality for the usage of graphene to selectively target cancer cells.

Keywords: lipids, reduced graphene oxide, cancer therapy, oxidative stress, human manganese superoxide dismutase, peroxidation

1. Introduction

Breast cancer is a frequently diagnosed malignancy in women and therapeutic goals aim to eradicate tumors and prevent their recurrence.^{1, 2} Although cancer therapy has improved with advances in anticancer drug development and cancer diagnostics for early detection, issues with drug resistance and adverse side effects limit the effectiveness of some treatments. Combination therapy holds promise for overcoming resistance to cancer treatment and for providing a better prognosis for cancer patients. This form of therapy utilizes multiple techniques to eliminate cancer cells by instigating different mechanisms of cell death to inhibit the ability of cancer cells to evade treatment. A substrate that is conducive to combination therapy and that holds the potential for delivering maximum therapeutic power is graphene.³⁻⁵

Graphene has been proposed as a substrate for cancer therapy due to its distinct high surface area, atomic thickness, and photothermal properties.⁶⁻⁸ Moreover, its capability to efficiently load high amounts of anticancer drugs and other cancer-fighting molecules make graphene an ideal platform for combination treatment against cancer. Previous studies of bare and modified graphene and graphene oxide demonstrated the strong potential of these materials to hinder proliferation of tumor cells, including lung⁵, breast^{5, 9}, and cervical¹⁰ cancers, but further evaluation of the effects of oxidative stress in both healthy and cancer cells is needed to better understand the interactions of 2D materials with tumorigenic and non-tumorigenic tissue.^{3, 5, 11-13} Additionally, the use of graphene as a delivery vehicle for chemotherapy can result in toxic side effects to healthy tissue due to the non-specific release of cytotoxic agents observed in previous work.^{3, 5} To prevent detrimental effects on healthy, surrounding tissue, it is crucial to develop a treatment strategy capable of targeting cancer cells.

The addition of lipids to graphene, reduced graphene oxide (rGO) used in this study, allows for enhanced biocompatibility and also expanded modes of functionality. Lipids allow for the attachment and loading of a variety of components including proteins, drugs, and cell penetrating peptides, making lipid-functionalized graphene capable of performing combination therapy and cell targeting. Liposome-based carriers have demonstrated considerable success as therapeutic vehicles due to their low toxicity, ability to target specific cells, increased therapeutic efficiency, and capacity to load different types of drugs. Lipid-functionalized graphene encompasses all of the advantages of liposomal drug delivery with the additional benefits of photothermal properties and higher surface to volume ratio. Prior studies have examined lipid-functionalized rGO and graphene oxide as a viable platform for sensing and drug delivery. Although lipid-functionalized rGO showed promising results for anticancer drug loading using the high loading

capacity of rGO and the ability for controlled release of drug in aqueous solutions, this platform was not evaluated with cells.²⁸

Oxidative stress plays an important role in cancer development, progression, and treatment. Cancer cells typically have significantly higher concentrations of reactive oxygen species (ROS) and lower antioxidant enzyme activity compared to healthy cells. The imbalance of ROS production and ROS removal has various adverse effects on cells, including lipid peroxidation, DNA mutations, and damaged protein function. The substantial difference in oxidative stress between tumorigenic and non-tumorigenic cells can result in divergent responses following exposure to 2D materials and can potentially be utilized to selectively induce cell death in cancer cells. Furthermore, it is important to characterize responses of both healthy and cancerous cells because nano-medicine is still not entirely specific to cancer cells and can cause negative side effects in normal tissue.²⁹⁻³¹

One type of ROS proposed to facilitate mutations in healthy cells and metastasis in cancer cells is superoxide. Human manganese superoxide dismutase (hMnSOD) has demonstrated effectiveness as a tumor suppressor in a variety of cell types, including breast cells.³²⁻³⁴ The mechanism controlling the ability of hMnSOD to fight cancer is not fully understood, but previous studies have suggested that this antioxidant enzyme protects against cancer progression by increasing hydrogen peroxide production and the expression of the tumor suppressor maspin.^{32, 35-37} The incorporation of hMnSOD onto lipid-rGO structures expands the therapeutic ability of lipid-rGO, and we hypothesize that naturally occurring hMnSOD will have less severe side effects on healthy cells than chemotherapeutics.

In this work, we examine the response of three breast cell lines: MCF-10A (non-tumorigenic), MCF-7 (cancerous, estrogen receptor positive), and MDA-MB-231 (triple negative,

metastatic) to bare and lipid-functionalized rGO. We demonstrate that each cell line has unique proliferation, cytotoxicity, and oxidative stress responses following exposure to bare and lipid-coated rGO and show the therapeutic benefits of hMnSOD connected to this engineered material (Figure 1). Interestingly, lipid-rGO structures reduced cell proliferation only in cancerous cell lines, and this correlated with peroxidation of the lipids coating rGO nanostructures that were in contact with the tumorigenic cells. Functionalization of lipid-rGO nanostructures with hMnSOD significantly inhibited growth of metastatic breast cancer cells while minimizing side effects on healthy cells and ROS involved in lipid peroxidation.

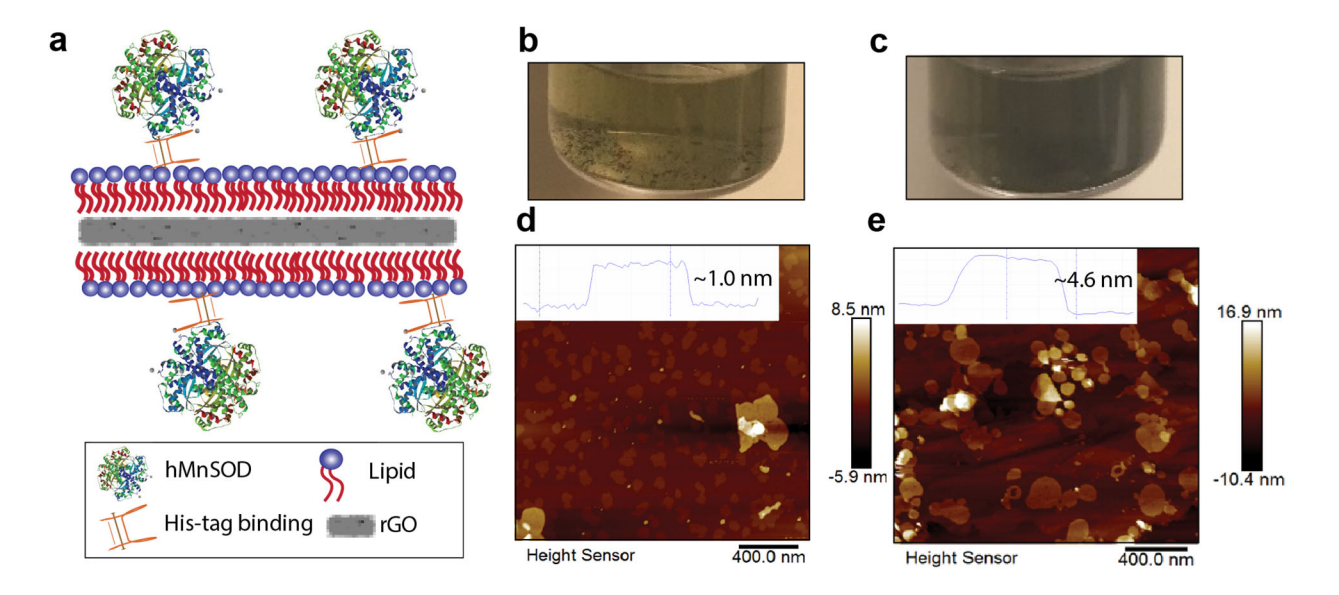


Figure 1. Characterization of lipid-rGO structures. a) Schematic depiction of hMnSOD attached to lipid-rGO. rGO is coated with lipid monolayers and hMnSOD binds through a 6×His-tag to lipid head groups modified with Ni-NTA. b) Bare rGO following sonication in Nanopure water has poor dispersion. c) Lipid-functionalized rGO formed from sonication of bare rGO with lipid vesicles results in enhanced solubility of rGO. d) Atomic force microscopy (AFM) micrograph of bare rGO after sonication. Inset shows an example line scan to evaluate the height of the bare rGO. The height of rGO flakes range from 1.4 ± 0.5 nm depending on the number of graphene layers on each flake, and the width of the flakes were 97 ± 27 nm. e) AFM micrographs of lipid-rGO structures. The height of lipid-rGO ranges from 4.8 ± 0.8 nm indicating lipid monolayer formation on each side of the rGO flakes. The width of the lipid-rGO structures was determined to be 89 ± 48 nm.

2. Materials and Methods

2.1 Synthesis of Lipid Vesicles

Lipid powders for 1-palmitoyl-2-oleoyl-sn-glycero-3-phosphocholine (POPC), 1,2-distearoyl-sn-glycero-3-phosphoethanolamine-N-[maleimide(polyethylene glycol)-2000] (DSPE-PEG2000 maleimide), and 1,2-dioleoyl-sn-glycero-3-[(N-(5-amino-1-carboxypentyl))iminodiacetic acid)succinyl] (nickel salt) (18:1) DGS-NTA (Ni) were purchased from Avanti Polar Lipids. Vesicles containing different concentrations of POPC, DGS-NTA, and DSPE-PEG2000 maleimide were prepared using the film hydration method. Lipids were suspended in chloroform at a concentration 25 mg/mL for POPC and 5 mg/mL for DGS-NTA (Ni) and DSPE-PEG2000 maleimide. The chloroform was then removed using a rotary evaporator with a water bath at 40 °C followed by further drying under vacuum to ensure complete removal of chloroform. The lipid film was rehydrated with phosphate buffered saline (PBS) at a pH 7.4. The solution was then extruded through a 200 nm track-etched membrane using a LIPEX extruder to create unilamellar vesicles. Vesicle size was verified with dynamic light scattering (DLS) using a Malvern Zetasizer Nano Series ZS90, and the average vesicle diameter was determined to be 180 ± 9.5 nm (Figure S1).

For experiments with bare and lipid-rGO structures, lipid vesicles were assembled with 98.8 mol% POPC, 0.2 mol% DSPE-PEG₂₀₀₀ maleimide, and 1 mol% DGS-NTA (Ni). For the lipid peroxidation assay, BODIPY 581/591 was incorporated into the vesicles at 0.15 mol%. Experiments involving hMnSOD binding to lipid-rGO structures used lipid vesicles containing 98.8 mol% POPC, 0.2 mol% DSPE-PEG₂₀₀₀ maleimide, and 1 mol% DGS-NTA (Ni) and vesicles with 94 mol% POPC, 5 mol% DSPE-PEG₂₀₀₀ maleimide, and 1 mol% DGS-NTA (Ni).

2.2 Preparation of Lipid-rGO and Bare rGO

The rGO used in this study was purchased from Graphenea. As reported by the manufacturer, the rGO used had an electrical conductivity of 6,667 S/m, and a BET surface area ranging from 422.69-499.85 m²/g. The elemental composition of the rGO powder was 77-87% carbon, 13-22% oxygen, and contained trace amounts of hydrogen and nitrogen. Lipid-rGO nanostructures were prepared using a previously published protocol with some modifications.²³ In brief, 0.5 mg/mL of rGO in Nanopure water was sonicated for 1 hour. The sonicated rGO was then mixed with lipid vesicle solution and placed in an ice bath and sonicated in a VWR bath sonicator for an additional 2 hours. Following sonication, the lipid-rGO solution was centrifuged at 5,000 rpm for 15 minutes to remove rGO aggregates. The resulting supernatant containing the stable lipid-rGO assemblies was utilized for experiments. The rGO aggregates were collected by centrifuging at 13,400 rpm for 2 minutes, dried, and weighed to determine the amount of rGO in the lipid-rGO nanostructures. Lipid-rGO structures were concentrated prior to addition to cells using 30 kDa centrifugal filters, and the concentration of rGO in the lipid-rGO structures was calculated using the volume of the concentrated lipid-rGO and the mass of rGO in the structures. Bare rGO was prepared by sonicating rGO in a DMSO solution for 1 hour to obtain higher dispersion of rGO. Concentrations of 1 mg/mL, 5 mg/mL, and 10 mg/mL rGO were prepared in DMSO to add to cells at a final concentration of 10, 50, and 100 µg/mL respectively, and all concentrations of rGO were added to cells in a 1% (v/v) DMSO solution.

2.3 Atomic force microscopy

Atomic force microscopy (AFM) experiments were carried out in air on a Bruker Icon Instrument in PeakForce tapping mode. Measurements were performed using a ScanAsyst Air tip with a spring constant of 0.4 N/m. The force used was 750 pN or lower for lipid-rGO samples to

avoid damaging the lipid-rGO structures. The images acquired used scan rates of 0.5 Hz and 512 pixels/line. The obtained images were then plane-fit to the first order to account for sample tilt, and the heights and widths of bare rGO and lipid-rGO were evaluated using line scans throughout the image.

2.4 Cell culture

The human breast cancer cell lines MDA-MB-231 (HTB-26) and MCF-7 (HTB-22) and the non-tumorigenic human breast cell line MCF-10A (CRL-10317) were obtained from the American Type Culture Collection (ATCC). MDA-MB-231 cells were cultured in Dulbecco's Modified Eagle's Medium (Corning) supplemented with 10% fetal bovine serum (FBS; Atlanta Biologicals) and 2% penicillin/streptomycin (5,000 U penicillin and 5 mg/mL streptomycin). The MCF-7 line was maintained in Eagle's Minimum Essential Medium (Corning) supplemented with 10% FBS, 2% penicillin/streptomycin, and 0.01 mg/mL human insulin (Sigma). The MCF-10A line was cultured in Mammary Epithelium Basal Medium (Lonza) supplemented with 2% penicillin/streptomycin and bovine pituitary extract (BPE), human epidermal growth factor (hEGF), insulin, and hydrocortisone aliquots from the MEGM Mammary Epithelial Cell Growth Medium BulletKit (Lonza). Media was replaced every 3-4 days for MDA-MB-231 and MCF-7 cells, and the media was changed every 2-3 days for MCF-10A cells. All cell lines were cultured at 37°C in a humidified 5% CO₂ atmosphere.

For microplate assays (LIVE/DEAD, MTS, DCFDA, and BODIPY 581/591), MCF-7 and MCF-10A cells were cultured in 96 well plates at a density of 12,500 cells per well. MDA-MB-231 cells were cultured in a 96 well plate at a density of 10,000 cells per well. The following treatments were added after the cells were incubated in phenol red-free media at different time intervals: bare-rGO and lipid-rGO at concentrations of 0, 10, 50, and 100 µg/mL. The control for

bare rGO (0 μ g/mL) contained the same volume of DMSO as the 10-100 μ g/mL samples to account for any cytotoxic effects from the DMSO.

2.5 Expression and Purification of Human Manganese Superoxide Dismutase

The plasmid containing the mature amino acid sequence for the human manganese superoxide dismutase (hMnSOD) gene was purchased from GenScript, created by gene synthesis. The sequence was codon-optimized for growth in Escherichia coli (E. coli), and a 6×His-tag was incorporated at the N-terminus for purification and future attachment to Ni-NTA lipids. The plasmid was transformed into E. coli strain Lemo21(DE3) (New England Biolabs Inc.) for growth and expression. E. coli was grown and purified similar to a previously published protocol with some modifications. Buffer compositions were: lysis buffer (50 mM potassium phosphate, 300 mM NaCl, 10 mM imidazole, 10 % glycerol, pH 7.8), wash buffer (50 mM potassium phosphate, 300 mM NaCl, 20 mM imidazole, pH 7.8, 10% glycerol), elution buffer (50 mM potassium phosphate, 300 mM NaCl, 250 mM imidazole, pH 7.8, 10% glycerol), and final protein buffer (50 mM potassium phosphate, 150 mM NaCl, pH 7.8 20% glycerol). Buffer exchange and concentration of hMnSOD following purification was performed using Amicon Ultra 0.5 mL centrifugal tubes of 30 kDa. Concentration and purity of purified hMnSOD was evaluated using the Bradford assay (VWR) and an SDS-PAGE gel (Figure S2) containing 12% acrylamide following a protocol from Cold Spring Harbor.³⁸

2.6 LIVE/DEAD assay for cytotoxicity

The ThermoFisher LIVE/DEAD Viability/Cytotoxicity Kit was used to assess cell cytotoxicity through the use of two fluorescent dyes to determine intracellular esterase activity and the integrity of plasma membranes. Calcein AM is converted enzymatically to the fluorescent calcein, producing a green fluorescence in live cells (ex/em: 495nm/515 nm) that confirms

intracellular esterase activity. Cells with damaged membranes are able to absorb ethidium homodimer (EthD-1), which then binds to nucleic acids. This interaction increases the fluorescence of EthD-1, making dead cells easily distinguishable by their red fluorescence (ex/em: 495 nm/635 nm). This assay was performed following the manufacturer's protocol. The optimal dye concentrations for calcein AM and EthD-1 were determined to be 0.5 μ M and 4 μ M, respectively. Fluorescence measurements were taken using a microplate reader (Infinite 200Pro). The gain was set to the optimal value using the microplate reader software. This optimal gain was then used for all samples, and the percentage of dead cells was calculated following the manufacturer's suggested protocol. All experiments were performed in at least triplicate with 3-4 repeat wells in each set of samples. The percentage of dead cells for each treatment is reported as mean \pm standard deviation.

2.7 MTS assay for cell proliferation

An Abcam MTS assay was used to determine cell proliferation by measuring the absorbance of the formazan dye product produced from the reduction of the MTS tetrazolium compound by viable cells. Following incubation of the cells with bare and lipid-rGO, each well was washed three times with 200 μ L phenol red-free media, and then 20 μ L Abcam MTS reagent was added to 200 μ L fresh media in each well. Cells were then incubated for one hour with the reagent in standard cell culture conditions. A microplate reader (Infinite 200Pro) was used to determine the absorbance of formazan at 490 nm with a reference wavelength of 650 nm. All experiments were run in triplicate with 3-4 wells in each set of samples. The absorbances for sample wells with the same treatment were averaged and then normalized to the control. Data are reported as mean \pm standard deviation.

2.8 DCFDA assay for oxidative stress

2',7'-dichlorofluorescin diacetate (DCFDA) was used to measure general ROS concentrations. DCFDA is cell permeable and becomes the highly fluorescent compound DCF following oxidation by various types of ROS. Oxidative stress was assessed by monitoring the increase in fluorescence of DCF (ex/em: 485 nm/ 535 nm) for a maximum of six hours following staining using an Abcam DCFDA Cellular ROS Detection Assay Kit. Cells were cultured in 200 μL phenol red-free media for 24 hours. The wells were washed with 100 μL 1× buffer, diluted from the 10× buffer from the Abcam DCFDA Cellular ROS Detection Assay Kit. Cells were then incubated with 20 μM DCFDA diluted in 1× buffer in the dark at 37 °C for 45 minutes. The DCFDA solution was then removed and cells were rinsed twice with 100 μL phenol red-free media. Bare and lipid-rGO structures were then added to the cells to final concentrations of 0, 10, 50, and 100 μg/mL. Fluorescence was measured immediately using a microplate reader (Infinite 200Pro) with 485 nm excitation and 535 nm emission filters and monitored for six hours. All treatments were run in triplicate with each run containing 4 wells. The fluorescence for each treatment was normalized to the control, averaged, and the standard deviation was calculated.

2.9 Protein Activity: NBT Inhibition Assay

Protein activity for hMnSOD was assessed using the nitroblue tetrazolium (NBT) inhibition assay. The yellow-colored, water-soluble NBT is reduced by superoxide to generate blue formazan, which can be measured spectrophotometrically. To determine the activity, various concentrations of hMnSOD were well-mixed in a cuvette with 1 mL NBT assay solution (Sigma) containing 67 mM potassium-phosphate buffer (pH 7.8), 1.5 mM NBT, 0.12 mM riboflavin, and 28 mM tetramethylethylenediamine (TEMED). One mL of NBT assay solution without hMnSOD was utilized as a control. The cuvettes were exposed equally to a fluorescent lamp, and after 30

seconds the reduction of NBT in the cuvettes was measured at 560 nm using a NanoDrop 2000c spectrophotometer for roughly six minutes to obtain multiple data points in the linear range for A₅₆₀. The absorbance at 560 nm was plotted as a function of time, and the slopes for the control and protein samples were calculated. The slopes for absorbance as a function of time correspond to the degree of NBT inhibition, with a higher slope indicating a greater amount of NBT reacting with superoxide. The percentage of NBT inhibition is calculated from:

% NBT inhibition =
$$\frac{m_{control} - m_{sample}}{m_{control}} \times 100$$

where m is the slope of the line for absorbance as a function of time. For the activity of the enzyme, one unit of protein is defined as the amount of protein needed to achieve 50% NBT inhibition.

2.10 Statistical Analysis

All experiments were performed in triplicate unless otherwise indicated. The data was represented as the mean \pm standard deviation. To determine statistical significance, t-tests were used with a 95% confidence interval (p < 0.05).

3. Results and Discussion

3.1 Formation and characterization of lipid-rGO structures

Graphene provides several advantages for cancer treatment in comparison to other platforms, such as high surface area for efficient loading of cancer-fighting molecules and its photothermal therapy capability. Functionalization of the surface of graphene increases biocompatibility of the material and allows for the incorporation of targeting chemical moieties, anticancer drugs, and other therapeutic molecules. Here, graphene was functionalized with lipid molecules using a previously established protocol. Bare rGO was first sonicated to disperse large aggregates of rGO and then was combined with lipid vesicles and sonicated again. Due to

hydrophobic interactions, lipid tails interact with the hydrophobic surface of the rGO to form a lipid monolayer coating the surfaces of the rGO (**Figure 1a**). Lipid-rGO structures were characterized by solubility and atomic force microscopy (AFM) (**Figure 1b-e**). Bare rGO displayed poor solubility in water following sonication and the solution visibly contained aggregates of rGO (**Figure 1b**). After sonication of bare rGO with lipid vesicles, improved solubility was observed (**Figure 1c**). AFM scans for bare and lipid-rGO revealed heights ranging from 1.4 ± 0.5 nm for bare graphene flakes and 4.8 ± 0.8 nm for lipid-rGO structures (**Figure 1d,e**). Widths for the bare rGO and lipid-rGO structures were determined to be 97 ± 27 nm and 89 ± 48 nm respectively. The addition of approximately four nm in height after sonication of lipid vesicles with rGO and the drastic increase in rGO solubility suggests the formation of a lipid monolayer on both sides of the 2D material, as similarly observed from prior studies that used this strategy. 23,28,39

3.2 Cell cytotoxicity and proliferation

When evaluating a platform for cancer treatment, it is essential to examine the effects of the platform on proliferation and cytotoxicity of both normal and tumorigenic tissues to ensure that detrimental side effects on healthy cells are minimized. Three cell lines, MCF-10A, MCF-7, and MDA-MB-231, were used in this study to represent healthy and cancerous breast tissue as well as different levels of cancer aggression. MCF-10A is a non-tumorigenic human breast cell line. MCF-7 is a non-metastatic, estrogen receptor-positive breast cancer cell line, and MDA-MB-231 is a triple negative, metastatic breast cancer cell line. MCF-10A, MCF-7, and MDA-MB-231 cells were incubated with varying concentrations of bare and lipid-functionalized rGO for 1 or 2 days, and then cell cytotoxicity and proliferation were evaluated. The controls for both cytotoxicity

and proliferation assays contained no rGO (0 μ g/mL), with the control for bare rGO containing the same concentration of DMSO (1% v/v) that was used as a carrier to solubilize the rGO.

To examine the effects of bare and lipid-rGO on cell death, we utilized a LIVE/DEAD assay. This assay uses two dyes to classify cells as alive (calcein AM) or dead (ethidium homodimer-1). Ethidium homodimer-1 (EthD-1) is only able to enter the cell upon membrane damage, a feature linked to necrosis, and therefore, the dead/EthD-1 stained cells are often classified as necrotic cells. 40-42 From the LIVE/DEAD assay, MCF-10A and MCF-7 cells demonstrated no change in cytotoxicity with increasing concentration of bare and lipid-rGO when compared to control samples, indicating no increase in detectable membrane damage following exposure to bare and lipid-rGO (Figure 2a,b). In contrast, high concentrations of bare and lipidrGO resulted in an approximately three-fold increase in cell death in MDA-MB-231 cells in comparison to control samples (Figure 2c). Several studies have demonstrated that cancer cells can utilize necrosis to enhance their proliferation and survival. ⁴³⁻⁴⁵ Apoptosis as opposed to necrosis is generally considered the preferred method of cell death for cancer therapeutics, although other mechanisms of cell death are being explored. 44, 46, 47 To avoid unwanted side effects on nearby tissue and to inhibit cancer progression associated with elevated necrosis, lipid-rGO structures must be modified or used at low concentrations so that they do not trigger necrosis in MDA-MB-231 cells.

To further explore the influence of bare and lipid-rGO on normal and malignant breast cells, cell proliferation was examined for all cell lines using the MTS assay. Bare rGO decreased cell proliferation in all cell lines with a greater reduction in cell division resulting from higher concentrations of rGO (**Figure 2d-f**). In contrast to bare rGO treatments, lipid-rGO evoked differential responses depending on the cell lines used. When the non-tumorigenic MCF-10A

breast cells were incubated with lipid-rGO structures, most lipid-rGO concentrations had no effect on proliferation, with only 100 μg/mL lipid-rGO significantly decreasing cell proliferation after one day when compared to the control 0 μg/ml lipid-rGO sample (**Figure 2d**). Conversely, the breast cancer cell lines, MCF-7 and MDA-MB-231, demonstrated a significant decline in cell proliferation following two days of incubation with lipid-rGO at concentrations of 50 μg/mL and 100 μg/mL, with a large reduction in cell growth occurring between day 1 and day 2 (**Figure 2 e,f**). These findings suggest unique responses to lipid-rGO nanostructures based on the tumorigenic state of the breast cells. Lipid-rGO structures significantly inhibited cell proliferation after two days for cancerous breast cell lines, whereas lipid-rGO had a negligible effect on cell proliferation in the non-tumorigenic cell line during this time period. These findings suggest that lipid-rGO structures can selectively reduce the growth rate of tumor cells.

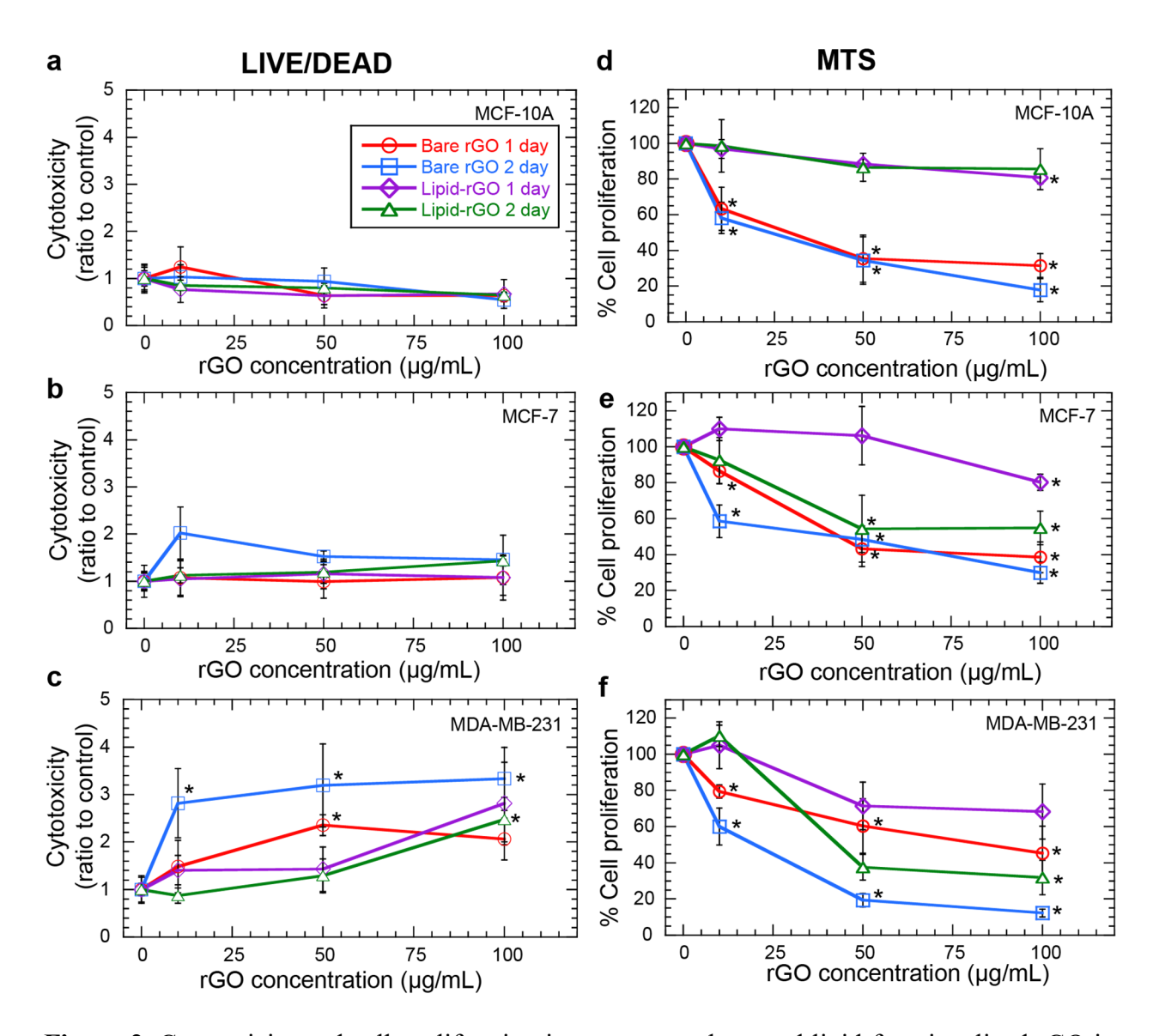


Figure 2. Cytotoxicity and cell proliferation in response to bare and lipid-functionalized rGO in cancerous and non-cancerous cells. LIVE/DEAD assay results analyzing cytotoxicity for a) MCF-10A, b) MCF-7, and c) MDA-MB-231 cell lines. All concentrations of bare rGO and 100 μ g/mL of lipid-rGO at 2 days of treatment caused a significant increase in death of MDA-MB-231 cells in comparison to the control. MCF-7 and MCF-10A cells did not demonstrate increased cytotoxicity for any concentration of bare or lipid-rGO in comparison to control wells. MTS assay results for cell proliferation for d) MCF-10A, e) MCF-7, and f) MDA-MB-231 cells. The cell proliferation for each sample was normalized to the control (0 μ g/mL rGO), with the control for bare rGO treatments containing the same concentration of DMSO of 1% (v/v). Error bars represent the standard deviation from at least three experiments. *p < 0.05 compared to the control samples for bare and lipid-rGO structures.

3.3 Oxidative stress and lipid peroxidation

To determine what factors influenced the decline in cell proliferation in breast cancer cells but not healthy breast cells, we examined oxidative stress in the cells in response to bare and lipidmodified rGO. Oxidative stress has been proposed to play a major role in cancer development and progression, and the extent of oxidative stress and cellular responses in normal and cancerous tissue often differs considerably, with cancer cells typically having much higher levels of ROS compared to healthy cells. 33, 48, 49 To analyze ROS generation after exposure to bare and lipid-rGO structures, the DCFDA assay was utilized (Figure 3). This assay uses a cell permeant dye that is oxidized upon interaction with various species of ROS to evaluate the overall level of oxidative stress experienced by the cells relative to the control (no added treatment) for each cell line. Incubation of cells with bare rGO caused a time-dependent increase in oxidative stress in all cell lines, while incubation with lipid-rGO nanostructures tempered the increase in ROS in comparison to the bare rGO. Interestingly, each cell line demonstrated a distinct profile of oxidative stress. In MDA-MB-231 cells, the levels of oxidative stress for 50 and 100 µg/mL of bare and lipid-rGO increased steadily for six hours. Conversely, both MCF-7 and MCF-10A cells exhibited a peak in oxidative stress in response to high concentrations of bare rGO during the six-hour period of the assay, with the peak of oxidative stress in MCF-10A cells occurring at approximately three hours earlier then in MCF-7 cells. This assay indicates that MCF-10A and MCF-7 cells might be able to better regulate ROS levels compared to MDA-MB-231 cells, because the maximum oxidative stress increase for MDA-MB-231 cells presumably occurs beyond the time frame of this assay. Due to the large increase of oxidative stress for all cell lines in response to bare rGO, unfunctionalized rGO was deemed to not be a viable material for breast cancer treatment. The considerable spike of ROS results in greater risk of mutations in non-tumorigenic tissue. Compared to bare rGO, the slight elevation in oxidative stress for MCF-10A following exposure of lipid-rGO structures is more conducive to a safe and effective cancer treatment.

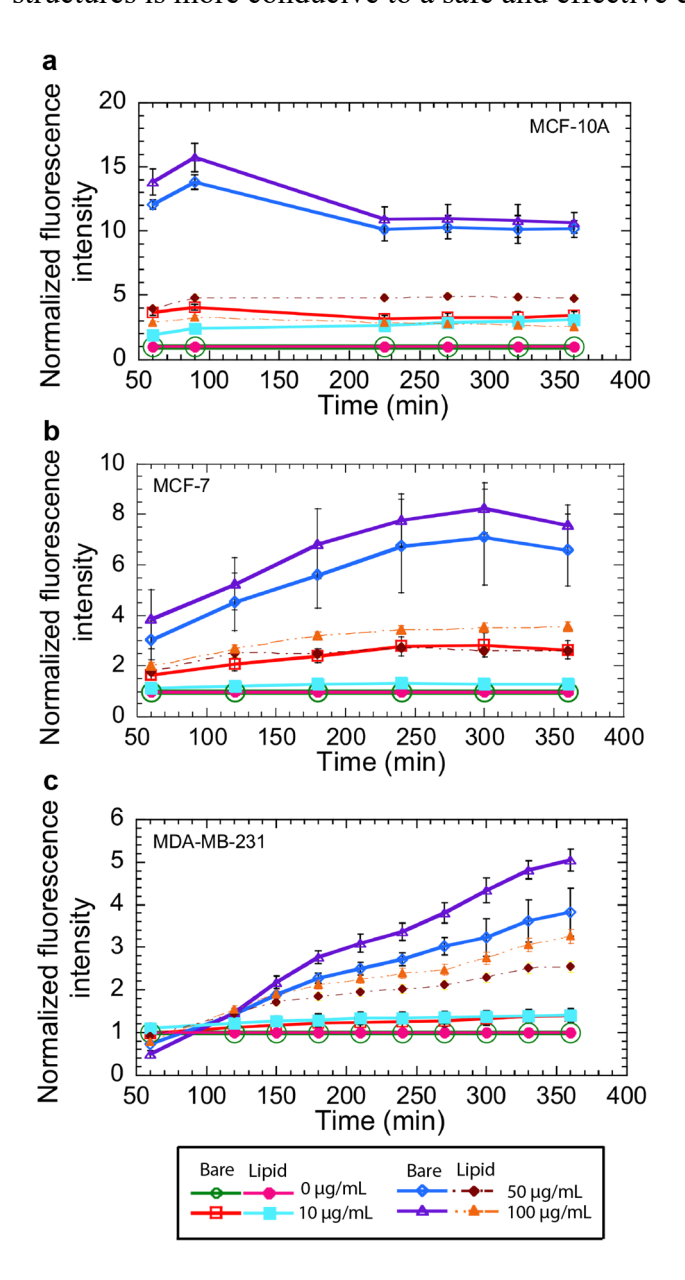


Figure 3. DCFDA assay used to measure oxidative stress following incubation of MCF-10A, MCF-7, and MDA-MB-231 with bare and lipid-functionalized rGO. This assay indicated different time profiles of ROS generation for the three cell lines. Each sample was normalized to the control (0 μg/mL rGO), representing the relative amount of oxidative stress for each cell line. Time progression of ROS generation for six hours post-addition of bare and lipid-rGO for a) MCF-10A, b) MCF-7, and c) MDA-MB-231 cells. Error bars represent the standard deviation from three experiments.

High oxidative stress can lead to the damage of multiple components in cells, including DNA, proteins, and lipids. In addition, elevated levels of ROS can result in increased rates of lipid peroxidation and disruption of cell membranes. To further study the influence of ROS levels after the introduction of lipid-rGO structures, the extent of lipid peroxidation for the lipids coating rGO was measured. BODIPY 581/591 was incorporated into the lipid coating on the rGO nanostructures and then the lipid-rGO structures were added to the cells to monitor the rate of lipid peroxidation. The concentration of rGO used for this experiment was 50 µg/mL; this concentration of lipid-rGO caused a significant reduction in cell proliferation for the two cancer cell types. The emission peak at 591 nm decays as the dye is oxidized and indicates lipid peroxidation. The control used for this lipid peroxidation study was lipid-rGO structures containing BODIPY 581/591 in the absence of cells in the respective media for each cell line. Lipid-rGO nanostructures incubated with MCF-10A cells demonstrated minimal lipid peroxidation over a 72 hour period (Figure 4a). In contrast, incubation of lipid functionalized-rGO with MDA-MB-231 and MCF-7 cells resulted in a decline in fluorescence at 591 nm of the BODIPY molecule indicating a high amount of lipid peroxidation.

The differences in the rate of lipid peroxidation correlates with the substantial decrease in cell proliferation between 1 and 2 days for cancerous cells incubated with lipid-rGO and the different responses in cell proliferation for lipid-rGO in non-tumorigenic and tumorigenic breast cells. This trend demonstrates that a greater decline in fluorescence at 590 nm of BODIPY 581/591, indicative of lipid peroxidation on lipid-rGO nanostructures, corresponds to a larger decrease in cell proliferation when compared to the control. MCF10-A cells present negligible lipid peroxidation and reduction in cell proliferation, whereas cancer cell lines, MCF-7 and MDA-MB-231, show decreasing cell division with increasing amount of peroxidized lipids. When lipids

become oxidized, they have the ability to hydrogen bond with water molecules, which can change their orientation as they rearrange themselves to interact with water. Altered lipid tail bonding weakens the hydrophobic interactions between the once highly hydrophobic tails of the lipids and the hydrophobic surface of rGO, likely resulting in the degradation of the lipid monolayers on either side of graphene and the transition of lipid-rGO to bare rGO (**Figure 4b**). This change in lipid orientation and decreased hydrophobic interactions can potentially expose bare rGO to the cells. The transition of lipid-rGO nanostructures to fully or partially bare rGO most likely causes the large decline of cell proliferation in cancer cells and the increase of necrotic cells in MDA-MB-231.

This finding additionally has implications for liposome-based drug delivery vehicles. From the higher levels of ROS and increased rate of lipid peroxidation in cancer cells, the lipid structure of liposomal drug carriers can deteriorate, causing premature delivery of drug and decreased specificity for release. It is vital that lipid-based drug carriers remain intact and leakproof until their target is reached in order to deliver maximum therapeutic ability and avoid unwanted side effects of the loaded anticancer drugs.

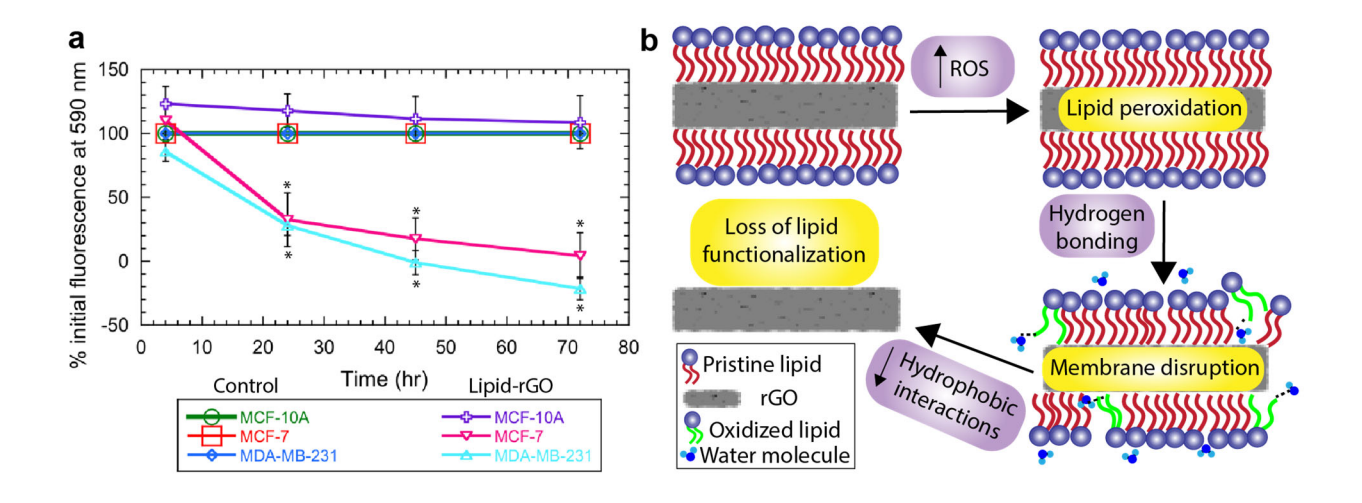


Figure 4. Lipid peroxidation leads to damage of lipid-rGO nanostructures resulting in possible exposure of bare rGO. a) Lipid peroxidation assay results for BODIPY 581/591-tagged lipid-rGO in breast cell lines for a 72-hour time frame. Error bars represent the standard deviation from three separate trials. *p < 0.05 compared to the control at the same time point. b) Model for the effect of lipid peroxidation on lipid-rGO assemblies. When the lipid-functionalized rGO is exposed to increased concentrations of ROS, such as with the breast cancer cell lines MCF-7 and MDA-MB-231, peroxidation of the lipids coating the rGO occurs to a much greater extent compared to the non-tumorigenic breast cell line, MCF-10A. Once the lipid tails have become oxidized, they have the ability to hydrogen bond with water molecules and alter their orientation. The decrease in hydrophobic interactions between the surface of rGO and lipid tails can potentially cause the lipid monolayers on both sides of the graphene to dissociate, resulting in the exposure of bare rGO.

3.4 Effect of free and bound hMnSOD on cell properties

Several prior studies have demonstrated that hMnSOD can act as a tumor suppressor in a variety of cancer cells, including breast cancer.^{32, 35-37} The overexpression of this naturally occurring protein has selectively hindered cell division in breast cancer cells.⁵⁵ Through the utilization of hMnSOD bound to lipid-rGO nanostructures, we aimed to inhibit the growth of cancerous breast cells with minimal side effects on non-tumorigenic breast cells and to reduce ROS involved in lipid peroxidation. To examine the capacity of hMnSOD as a breast cancer therapy, the activity of the purified protein and its effect on cell proliferation and viability were evaluated.

Following characterization and optimization of the activity of bound hMnSOD (**Figure S3**), the effects of free and bound hMnSOD on cell proliferation and cytotoxicity were evaluated. The control for these experiments did not contain hMnSOD or lipid-rGO structures. The concentration of lipid-rGO structures used for the loading of hMnSOD was 50 μg/mL of rGO. Incubation of MDA-MB-231 cells with free and bound enzyme results in a decrease in cell proliferation compared to the control (**Figure 5**). After one day, free and bound hMnSOD and lipid-rGO treated MDA-MB-231 cells displayed a similar level of reduction in cell division with a decline in cell proliferation to approximately 50% of the control. However, proliferation after

two days for MDA-MB-231 cells treated with lipid-rGO structures with and without attached hMnSOD was roughly 50% and 30% of the control value respectively, suggesting that hMnSOD has an impact on the lipid-rGO system and/or cell division. Lipid-rGO structures with hMnSOD were further examined in MDA-MB-231 cells, the only cell line to display increased necrosis from LIVE/DEAD assays, to determine their influence on cytotoxicity. Interestingly, when hMnSOD was bound to 100 μg/mL of lipid-rGO structures, no detectable increase in the percentage of necrotic cells was observed relative to the control, whereas lipid-rGO structures without hMnSOD resulted in elevated occurrence of necrosis as previously observed in initial LIVE/DEAD assays (**Figure 5b**). Because necrosis has been associated with tumor progression, the ability of hMnSOD to repress necrosis while inhibiting cell proliferation in metastatic cancer cells is important for blocking cancer progression. The presence of hMnSOD limited the degree of lipid peroxidation of the lipid coating on rGO (Figure 5c) most likely by minimizing the amount of protonated superoxide and hydroxyl radical, two of the main reactive oxygen species involved in lipid peroxidation that are present in this system. ⁵⁰⁻⁵² By decreasing the extent of lipid peroxidation of the functionalized rGO structures, it is likely that bare rGO is not exposed to the cells in the time frame examined, which could explain the differences in cellular responses of lipid-rGO structures with and without hMnSOD after two days. The reduction in necrosis and the steady reduction in cell division indicate that hMnSOD has a protective effect on the lipid-functionalization on bare rGO that can be advantageous for maintaining intact lipid-rGO systems, reducing the amount of necrotic cells, and inhibiting growth of metastatic breast cancer cells.

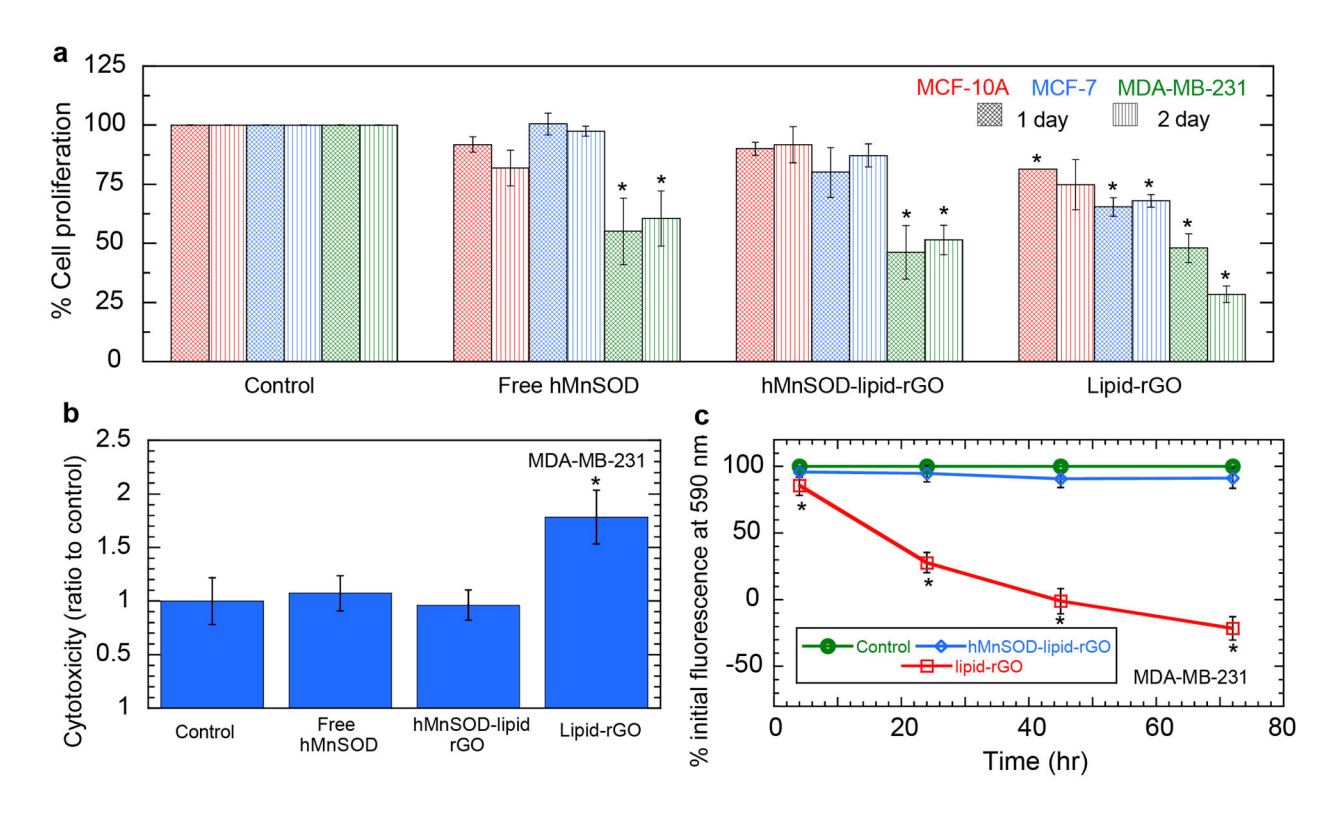


Figure 5. hMnSOD bound to lipid-rGO structures selectively reduces proliferation, necrosis, and lipid peroxidation in metastatic cancer cells (MDA-MB-231) while minimally affecting non-tumorigenic cells (MCF-10A). a) MTS assay data for MCF-10A, MCF-7, and MDA-MB-231 cells. b) LIVE/DEAD assay following 2 days incubation in MDA-MB-231 cells. c) Lipid peroxidation assay for the lipid coating of the lipid-rGO nanostructures in the presence and absence of hMnSOD incubated with MDA-MB-231 cells. The control used was lipid-rGO structures containing BODIPY 581/591 in the absence of cells in cell media. Error bars represent the standard deviation from at least three separate experiments. *p < 0.05 compared to the control.

Conversely, cell division of MCF-7 and MCF-10A cells was not affected by free and bound hMnSOD compared to the controls (**Figure 5a**). The differences in responses from the metastatic carcinoma cells (MDA-MB-231) compared to the less aggressive cancer line (MCF-7) and the non-tumorigenic cells (MCF-10A) may be due to the overall superoxide dismutase (SOD) levels in the cell lines. Prior studies have demonstrated a substantial difference in total SOD activity in MCF10-A, MCF-7, and MDA-MB-231 cell lines, with MCF-10A and MDA-MB-231 having the highest and lowest SOD activity respectively. Furthermore, the introduction of additional SOD has been used as a tumor suppressor in several studies. Consistent with these findings, our work shows

that increased hMnSOD has the highest impact on cell proliferation and viability of MDA-MB-231 cells, the cell line with the most downregulated SOD levels. Indeed, lipid-rGO functionalized with hMnSOD selectively reduced cell growth of metastatic breast cancer cells, avoided uncontrolled cell death, and likely preserved lipid-rGO nanostructures by preventing lipid peroxidation. Compared to doxorubicin, a commonly used anticancer drug, hMnSOD-lipid-rGO nanostructures reduced proliferation of the metastatic MDA-MB-231 breast cancer cells with no harmful effects on the non-tumorigenic MCF-10A breast cells. The ability of this platform to diminish growth of metastatic cancer cells has potential to decrease reliance on chemotherapy and prevent its negative reactions to normal tissue.

4. Conclusions

Healthy and tumorigenic breast cells exhibit differential responses following exposure to bare and lipid-functionalized rGO suggesting that the use of lipid-rGO structures may prove to be a useful platform for selective cancer treatment. Bare rGO instigated higher oxidative stress and decreased cell division in all cell lines and caused an increase in necrosis for metastatic MDA-MB-231 breast cancer cells. The heightened ROS production and reduced cell proliferation in both healthy and cancer cells from bare rGO make unfunctionalized rGO not suitable for cancer therapy. Although possibly valuable in eliminating cancer cells, increased generation of ROS and necrosis can harm the function of healthy cells and result in undesired side effects. Conversely, lipid-rGO structures did not affect cell proliferation and viability of MCF-10A cells and caused a minimal increase in ROS production and lipid peroxidation. The attachment of hMnSOD to lipid-rGO demonstrated multiple benefits for the lipid-functionalized graphene system due to its ability to impede cancer cell division without initiating necrosis and the lack of detrimental reactions with

healthy breast cells. This platform has significant potential to be used for cancer treatment because it selectively inhibits cell division of metastatic breast cancer cells and utilizes a natural enzyme for increased tumor suppressor activity and protection of the lipid-functionalization on rGO. hMnSOD attached to lipid-rGO structures used in conjunction with the photothermal effect may prove to be a highly potent and effective system in combination therapy for elimination of tumors.

Acknowledgements

This material is based upon work supported by the National Science Foundation Graduate Research Fellowship Program under Grant No. DGE1255832 and in part by NSF CBET-1552571 and NSF EEC-1659497. Any opinions, findings, and conclusions or recommendations expressed in this material are those of the author(s) and do not necessarily reflect the views of the National Science Foundation. We would like to acknowledge Dr. Andrew Zydney for the use of his microplate reader in this study.

Supporting Information Available: The following files are available free of charge: Optimization of the activity of hMnSOD bound to lipid-rGO structures. Supporting figures for dynamic light scattering of lipid vesicles, SDS-PAGE gel for hMnSOD, and hMnSOD activity assay data.

References

- 1. Harbeck, N.; Penault-Llorca, F.; Cortes, J.; Gnant, M.; Houssami, N.; Poortmans, P.; Ruddy, K.; Tsang, J.; Cardoso, F., Breast Cancer. *Nature Reviews Disease Primers* **2019**, *5* (1), 66.
- 2. Waks, A. G.; Winer, E. P., Breast Cancer Treatment: A Review. *Jama* **2019**, *321* (3), 288-300.
- 3. Cheon, Y. A.; Bae, J. H.; Chung, B. G., Reduced Graphene Oxide Nanosheet for Chemophotothermal Therapy. *Langmuir* **2016**, *32* (11), 2731-2736.
- 4. Shao, L.; Zhang, R.; Lu, J.; Zhao, C.; Deng, X.; Wu, Y., Mesoporous Silica Coated Polydopamine Functionalized Reduced Graphene Oxide for Synergistic Targeted Chemophotothermal Therapy. *ACS applied materials & interfaces* **2017**, *9* (2), 1226-1236.
- 5. Muthoosamy, K.; Abubakar, I. B.; Bai, R. G.; Loh, H.-S.; Manickam, S., Exceedingly Higher Co-loading of Curcumin and Paclitaxel onto Polymer-functionalized Reduced Graphene Oxide for Highly Potent Synergistic Anticancer Treatment. *Scientific reports* **2016**, *6*, 32808.
- 6. Zhang, Q.; Wu, Z.; Li, N.; Pu, Y.; Wang, B.; Zhang, T.; Tao, J., Advanced Review of Graphene-based Nanomaterials in Drug Delivery Systems: Synthesis, Modification, Toxicity and Application. *Materials Science and Engineering: C* **2017**, *77*, 1363-1375.
- 7. Liu, J.; Cui, L.; Losic, D., Graphene and Graphene Oxide as New Nanocarriers for Drug Delivery Applications. *Acta biomaterialia* **2013**, *9* (12), 9243-9257.
- 8. Yang, Y.; Asiri, A. M.; Tang, Z.; Du, D.; Lin, Y., Graphene Based Materials for Biomedical Applications. *Materials today* **2013**, *16* (10), 365-373.
- 9. Hu, S. H.; Chen, Y. W.; Hung, W. T.; Chen, I. W.; Chen, S. Y., Quantum-dot-tagged Reduced Graphene Oxide Nanocomposites for Bright Fluorescence Bioimaging and Photothermal Therapy Monitored In Situ. *Advanced materials* **2012**, *24* (13), 1748-1754.
- 10. Kim, H.; Lee, D.; Kim, J.; Kim, T.-i.; Kim, W. J., Photothermally Triggered Cytosolic Drug Delivery via Endosome Disruption Using a Functionalized Reduced Graphene Oxide. *ACS nano* **2013**, *7* (8), 6735-6746.
- 11. Chowdhury, S. M.; Lalwani, G.; Zhang, K.; Yang, J. Y.; Neville, K.; Sitharaman, B., Cell Specific Cytotoxicity and Uptake of Graphene Nanoribbons. *Biomaterials* **2013**, *34* (1), 283-293.
- 12. Chaudhari, N. S.; Pandey, A. P.; Patil, P. O.; Tekade, A. R.; Bari, S. B.; Deshmukh, P. K., Graphene Oxide Based Magnetic Nanocomposites for Efficient Treatment of Breast Cancer. *Materials Science and Engineering: C* **2014**, *37*, 278-285.
- 13. Yuan, X.; Liu, Z.; Guo, Z.; Ji, Y.; Jin, M.; Wang, X., Cellular Distribution and Cytotoxicity of Graphene Quantum Dots with Different Functional Groups. *Nanoscale research letters* **2014**, *9* (1), 108.
- 14. Chikh, G. G.; Li, W. M.; Schutze-Redelmeier, M.-P.; Meunier, J.-C.; Bally, M. B., Attaching Histidine-tagged Peptides and Proteins to Lipid-based Carriers through Use of Metalion-chelating Lipids. *Biochimica Et Biophysica Acta (BBA)-Biomembranes* **2002**, *1567*, 204-212.
- 15. Gao, H.; Zhang, Q.; Yu, Z.; He, Q., Cell-penetrating Peptide-based Intelligent Liposomal Systems for Enhanced Drug Delivery. *Current pharmaceutical biotechnology* **2014**, *15* (3), 210-219.

- 16. Colletier, J.-P.; Chaize, B.; Winterhalter, M.; Fournier, D., Protein Encapsulation in Liposomes: Efficiency Depends on Interactions between Protein and Phospholipid Bilayer. *BMC biotechnology* **2002**, *2* (1), 9.
- 17. Sercombe, L.; Veerati, T.; Moheimani, F.; Wu, S. Y.; Sood, A. K.; Hua, S., Advances and Challenges of Liposome Assisted Drug Delivery. *Frontiers in pharmacology* **2015**, *6*, 286.
- 18. Alavi, M.; Karimi, N.; Safaei, M., Application of Various Types of Liposomes in Drug Delivery Systems. *Advanced pharmaceutical bulletin* **2017**, *7* (1), 3.
- 19. Torchilin, V. P., Recent Advances with Liposomes as Pharmaceutical Carriers. *Nature reviews Drug discovery* **2005**, *4* (2), 145.
- 20. Farell, M.; Wetherington, M.; Shankla, M.; Chae, I.; Subramanian, S.; Kim, S. H.; Aksimentiev, A.; Robinson, J.; Kumar, M., Characterization of the Lipid Structure and Fluidity of Lipid Membranes on Epitaxial Graphene and Their Correlation to Graphene Features. *Langmuir* **2019**, *35* (13), 4726-4735.
- 21. Wang, Y. Y.; Pham, T. D.; Zand, K.; Li, J.; Burke, P. J., Charging the Quantum Capacitance of Graphene with a Single Biological Ion Channel. *Acs Nano* **2014**, *8* (5), 4228.
- 22. Thapa, R. K.; Byeon, J. H.; Choi, H.-G.; Yong, C. S.; Kim, J. O., PEGylated Lipid Bilayer-wrapped Nano-graphene Oxides for Synergistic Co-delivery of Doxorubicin and Rapamycin to Prevent Drug Resistance in Cancers. *Nanotechnology* **2017**, *28* (29), 295101.
- 23. Liu, S.-J.; Wen, Q.; Tang, L.-J.; Jiang, J.-H., Phospholipid–graphene Nanoassembly as a Fluorescence Biosensor for Sensitive Detection of Phospholipase D Activity. *Analytical chemistry* **2012**, *84* (14), 5944-5950.
- 24. Chen, P.; Yue, H.; Zhai, X.; Huang, Z.; Ma, G.-H.; Wei, W.; Yan, L.-T., Transport of a Graphene Nanosheet Sandwiched Inside Cell Membranes. *Science advances* **2019**, *5* (6), eaaw3192.
- 25. Gu, Z.; Zhu, S.; Yan, L.; Zhao, F.; Zhao, Y., Graphene-Based Smart Platforms for Combined Cancer Therapy. *Advanced Materials* **2019**, *31* (9), 1800662.
- 26. Liu, J.; Dong, J.; Zhang, T.; Peng, Q., Graphene-based Nanomaterials and Their Potentials in Advanced Drug Delivery and Cancer Therapy. *Journal of controlled release* **2018**, *286*, 64-73.
- 27. Jiang, W.; Mo, F.; Lin, Y.; Wang, X.; Xu, L.; Fu, F., Tumor Targeting Dual Stimuli Responsive Controllable Release Nanoplatform Based on DNA-conjugated Reduced Graphene Oxide for Chemo-photothermal Synergetic Cancer Therapy. *Journal of Materials Chemistry B* **2018**, *6* (26), 4360-4367.
- 28. Liu, J.; Guo, S.; Han, L.; Wang, T.; Hong, W.; Liu, Y.; Wang, E., Synthesis of Phospholipid Monolayer Membrane Functionalized Graphene for Drug Delivery. *Journal of Materials Chemistry* **2012**, *22* (38), 20634-20640.
- 29. Tran, S.; DeGiovanni, P.-J.; Piel, B.; Rai, P., Cancer Nanomedicine: A Review of Recent Success in Drug Delivery. *Clinical and translational medicine* **2017**, *6* (1), 44.
- 30. Iqbal, J.; Abbasi, B. A.; Ahmad, R.; Mahmood, T.; Ali, B.; Khalil, A. T.; Kanwal, S.; Shah, S. A.; Alam, M. M.; Badshah, H., Nanomedicines for Developing Cancer Nanotherapeutics: from Benchtop to Bedside and Beyond. *Applied microbiology and biotechnology* **2018**, *102* (22), 9449-9470.
- 31. Kydd, J.; Jadia, R.; Velpurisiva, P.; Gad, A.; Paliwal, S.; Rai, P., Targeting Strategies for the Combination Treatment of Cancer Using Drug Delivery Systems. *Pharmaceutics* **2017**, *9* (4), 46.

- 32. Weydert, C. J.; Waugh, T. A.; Ritchie, J. M.; Iyer, K. S.; Smith, J. L.; Li, L.; Spitz, D. R.; Oberley, L. W., Overexpression of Manganese or Copper–zinc Superoxide Dismutase Inhibits Breast Cancer Growth. *Free Radical Biology and Medicine* **2006**, *41* (2), 226-237.
- 33. Hecht, F.; Pessoa, C. F.; Gentile, L. B.; Rosenthal, D.; Carvalho, D. P.; Fortunato, R. S., The Role of Oxidative Stress on Breast Cancer Development and Therapy. *Tumor biology* **2016**, *37* (4), 4281-4291.
- 34. Karihtala, P.; Soini, Y., Reactive Oxygen Species and Antioxidant Mechanisms in Human Tissues and Their Relation to Malignancies. *Apmis* **2007**, *115* (2), 81-103.
- 35. Duan, H.; Zhang, H. J.; Yang, J.-Q.; Oberley, L. W.; Futscher, B. W.; Domann, F. E., MnSOD Up-regulates Maspin Tumor Suppressor Gene Expression in Human Breast and Prostate Cancer Cells. *Antioxidants and Redox Signaling* **2003**, *5* (5), 677-688.
- 36. Ridnour, L. A.; Oberley, T. D.; Oberley, L. W., Tumor Suppressive Effects of MnSOD Overexpression may Involve Imbalance in Peroxide Generation versus Peroxide Removal. *Antioxidants and Redox Signaling* **2004**, *6* (3), 501-512.
- 37. Teoh, M. L.; Fitzgerald, M. P.; Oberley, L. W.; Domann, F. E., Overexpression of Extracellular Superoxide Dismutase Attenuates Heparanase Expression and Inhibits Breast Carcinoma Cell Growth and Invasion. *Cancer research* **2009**, *69* (15), 6355-6363.
- 38. Sambrook, J.; Russell, D. W., SDS-polyacrylamide Gel Electrophoresis of Proteins. *CSH Protoc* **2006**, *2006* (4), pdb. prot4540.
- 39. Liu, J.; Han, L.; Wang, T.; Hong, W.; Liu, Y.; Wang, E., Enzyme Immobilization and Direct Electrochemistry Based on a New Matrix of Phospholipid-Monolayer-Functionalized Graphene. *Chemistry–An Asian Journal* **2012**, *7* (12), 2824-2829.
- 40. Edwards, J. R.; Diamantakos, E. A.; Peuler, J. D.; Lamar, P. C.; Prozialeck, W. C., A Novel Method for the Evaluation of Proximal Tubule Epithelial Cellular Necrosis in the Intact Rat Kidney Using Ethidium Homodimer. *BMC physiology* **2007**, *7* (1), 1.
- 41. Phimister, A. J.; Williams, K. J.; Van Winkle, L. S.; Plopper, C. G., Consequences of Abrupt Glutathione Depletion in Murine Clara Cells: Ultrastructural and Biochemical Investigations into the Role of Glutathione Loss in Naphthalene Cytotoxicity. *Journal of Pharmacology and Experimental Therapeutics* **2005**, *314* (2), 506-513.
- 42. Besenhofer, L. M.; Adegboyega, P. A.; Bartels, M.; Filary, M. J.; Perala, A. W.; McLaren, M. C.; McMartin, K. E., Inhibition of Metabolism of Diethylene Glycol Prevents Target Organ Toxicity in Rats. *Toxicological Sciences* **2010**, *117* (1), 25-35.
- 43. Karsch-Bluman, A.; Feiglin, A.; Arbib, E.; Stern, T.; Shoval, H.; Schwob, O.; Berger, M.; Benny, O., Tissue Necrosis and its Role in Cancer Progression. *Oncogene* **2019**, *38* (11), 1920.
- 44. Lee, S. Y.; Ju, M. K.; Jeon, H. M.; Jeong, E. K.; Lee, Y. J.; Kim, C. H.; Park, H. G.; Han, S. I.; Kang, H. S., Regulation of Tumor Progression by Programmed Necrosis. *Oxidative medicine and cellular longevity* **2018**, *2018*.
- 45. Bredholt, G.; Mannelqvist, M.; Stefansson, I. M.; Birkeland, E.; Bø, T. H.; Øyan, A. M.; Trovik, J.; Kalland, K.-H.; Jonassen, I.; Salvesen, H. B., Tumor Necrosis is an Important Hallmark of Aggressive Endometrial Cancer and Associates with Hypoxia, Angiogenesis and Inflammation Responses. *Oncotarget* **2015**, *6* (37), 39676.
- 46. Zhang, J.; Lou, X.; Jin, L.; Zhou, R.; Liu, S.; Xu, N.; Liao, D. J., Necrosis, and Then Stress Induced Necrosis-like Cell Death, but Not Apoptosis, Should be the Preferred Cell Death Mode for Chemotherapy: Clearance of a Few Misconceptions. *Oncoscience* **2014**, *1* (6), 407.
- 47. Su, Z.; Yang, Z.; Xu, Y.; Chen, Y.; Yu, Q., Apoptosis, Autophagy, Necroptosis, and Cancer Metastasis. *Molecular cancer* **2015**, *14* (1), 48.

- 48. Matés, J. M.; Segura, J. A.; Alonso, F. J.; Márquez, J., Intracellular Redox Status and Oxidative Stress: Implications for Cell Proliferation, Apoptosis, and Carcinogenesis. *Archives of toxicology* **2008**, *82* (5), 273-299.
- 49. Sosa, V.; Moliné, T.; Somoza, R.; Paciucci, R.; Kondoh, H.; LLeonart, M. E., Oxidative Stress and Cancer: An Overview. *Ageing research reviews* **2013**, *12* (1), 376-390.
- 50. Ayala, A.; Muñoz, M. F.; Argüelles, S., Lipid Peroxidation: Production, Metabolism, and Signaling Mechanisms of Malondialdehyde and 4-hydroxy-2-nonenal. *Oxidative medicine and cellular longevity* **2014**, *2014*.
- 51. McCord, J. M., Superoxide Dismutase, Lipid Peroxidation, and Bell-shaped Dose Response Curves. *Dose-Response* **2008**, *6* (3), dose-response. 08-012. McCord.
- 52. Gutteridge, J. M., Lipid Peroxidation Initiated by Superoxide-dependent Hydroxyl Radicals Using Complexed Iron and Hydrogen Peroxide. *FEBS letters* **1984**, *172* (2), 245-249.

TOC graphic:

